Food and Chemical Toxicology 206 (2025) 115743

Contents lists available at ScienceDirect

Food and Chemical Toxicology

journal homepage: www.elsevier.com/locate/foodchemtox

The potential mechanism of methamphetamine-induced mitochondrial dysfunction and cell degeneration via direct permeation across mitochondrial membranes: The study on molecular dynamics simulations and *in vitro* model

Tanthai Polvat [a,b], Wasinee Khuntawee [c], Tanya Prasertporn [a], Kornkanok Promthep [a], Nathanon Kerdkaen [c,e], Jiraporn Panmanee [a], Pornkamon Nalakarn [c,d], Jirasak Wong-ekkabut [c,e,*], Banthit Chetsawang [a,**]

[a] *Research Center for Neuroscience, Institute of Molecular Biosciences, Mahidol University, Salaya, Nakhon Pathom, 73170, Thailand*
[b] *Center of Emotional Health, Department of Psychology, Macquarie University, Balaclava Road, North Ryde, NSW, 2109, Australia*
[c] *Computational Biomodelling Laboratory for Agricultural Science and Technology (CBLAST), Faculty of Science, Kasetsart University, Bangkok, 10900, Thailand*
[d] *Department of Physics, Faculty of Science and Technology, Thammasat University, Pathumthani, 12120, Thailand*
[e] *Department of Physics, Faculty of Science, Kasetsart University, Bangkok, 10900, Thailand*

ARTICLE INFO

Handling Editor: Professor Matthew Wright

Keywords:
Methamphetamine
Dopamine
Phospholipid membrane
Apoptosis
Mitochondrial dysfunction
Molecular dynamics
Cell cultures

ABSTRACT

This study aims to investigate the direct permeation of methamphetamine (METH)-induced mitochondrial dysfunction leading to apoptotic cell death. The molecular dynamics (MD) simulations were performed to study METH and dopamine (DA) penetration through phospholipid membranes, which are abundant on the cellular and mitochondrial membranes. The simulation results showed that METH molecules passively diffuse into the membranes, whereas the DA molecule adsorbs onto the lipid bilayer interface. Additionally, the number of H-bond formations and the distribution lifetime of METH were higher than those of DA. Furthermore, the potential of mean force (PMF) profiles for METH and DA translocating through the lipid bilayer were calculated. The result demonstrated that the free energy barrier of METH is small, and the lowest free energy is located inside the bilayer. On the other hand, a significant energy barrier was found at the bilayer center in the PMF profile of DA. The simulation results suggest that METH can passively penetrate through the lipid bilayer. METH-induced mitochondrial dysfunction leading to cell death was observed in both dopamine transporter (DAT)-expressing cells and non-DAT-expressing cells. This finding highlights the direct permeation of METH across the membrane, inducing impairment of mitochondrial function and cell degeneration.

1. Introduction

Methamphetamine (METH) is a psychostimulant that has a chemical structure similar to monoamine neurotransmitters such as norepinephrine (NE), serotonin (5-HT) and dopamine (DA) with high lipid solubility to pass through the blood-brain barrier (BBB) and interact with various neural circuitry of the brain and causing drug addiction, neurodegeneration and cognitive dysfunction (Nordahl et al., 2003). Substantial evidence suggests that METH can be taken up via the dopamine transporter (DAT) and disrupt the dopaminergic system, leading to the accumulation of dopamine in presynaptic neurons and synaptic clefts. Furthermore, the dopamine overflow can initiate various neurotoxic effects, including DA autooxidation and increased reactive oxygen species (ROS) formation which disturb mitochondrial dynamics and initiate apoptotic processes (Shin et al., 2018; Yang et al., 2018). Moreover, several studies reported that METH can induce mitochondrial changes in astrocyte and microglial cell culture (Galluzzi et al., 2008), which might indicate non-DAT transport of METH into the cells and the direct non-DA-dependent toxic effect of METH in glial cells leading to cell apoptosis by the intrinsic mitochondrial pathway (D'Brant et al., 2019;

---

* Corresponding author. Computational Biomodelling Laboratory for Agricultural Science and Technology (CBLAST) and Department of Physics, Faculty of Science, Kasetsart University, Bangkok, 10900, Thailand.

** Corresponding author. Research Center for Neuroscience, Institute of Molecular Biosciences, Mahidol University, Salaya, Nakhon Pathom, 73170, Thailand.

E-mail addresses: jirasak.w@ku.th (J. Wong-ekkabut), banthit.che@mahidol.ac.th (B. Chetsawang).

https://doi.org/10.1016/j.fct.2025.115743
Received 28 June 2025; Received in revised form 14 September 2025; Accepted 14 September 2025

Sharikova et al., 2018). Recent evidence suggests that METH has cationic lipophilic properties that enable it to be directly diffused into the phospholipid bilayer, thereby interrupting mitochondrial membrane potential and pH (Davidson et al., 2001). However, there is still no scientific evidence to elucidate this phenomenon. Previous studies (Choudhary et al., 2024; Horvath and Daum, 2013) showed that the main phospholipids in mammalian cellular and mitochondrial membranes were phosphatidylcholine (PC), phosphatidylethanolamine (PE), and cardiolipin (CL). PC is the most abundant, comprising up to 40–44 % of total mitochondrial phospholipids, followed by PE at 27–34 %, and CL at 13–14 %. The outer mitochondrial membrane (OMM) has more PC (54 %) than the inner mitochondrial membrane (IMM) (40 %), while PE is slightly higher in the IMM (34 %) than the OMM (29 %). CL is mainly found in the IMM, comprising 18 % of its phospholipids. Additionally, the most common PC subtypes in brain tissue and brain mitochondrial membranes are 1-palmitoyl-2-oleoyl-glycero-3-phosphocholine (POPC) (25 % of all PC types) and dipalmitoyl phosphatidylcholine (DPPC) (10 % of all PC types), which form a significant portion of mitochondrial phospholipids and make them useful for studying drug permeation across mitochondrial membranes (Kuschner et al., 2018).

Therefore, this study aimed to investigate the potential of METH to passively permeate into the mitochondrial membrane. The interaction of METH with mitochondrial membrane potential leads to mitochondrial dysfunction and induces cell death in dopaminergic-like cell lines (SH-SY5Y cells) and non-neuronal cell lines (HEK 293T cells). Molecular dynamics (MD) simulations of METH and DA molecules were performed to study permeation in lipid bilayers. The POPC and DPPC bilayers were used as a simplified model of biological mitochondrial membranes. The free energy profiles of METH and DA translocation across the bilayer were investigated by using umbrella sampling simulations. Furthermore, an *in vitro* study was performed on both DAT-presenting cells and non-DAT-presenting cells to validate the potential of METH-induced mitochondrial membrane depolarization. The results could promote more understanding of the permeation of METH and DA through the membrane.

2. Materials and methods

2.1. Unbiased molecular dynamics simulation

The molecular dynamics (MD) simulations of DPPC and POPC lipid bilayers were performed to determine the behaviors and permeability of methamphetamine (METH) as a target ligand compared to dopamine (DA). The structures and force fields of DPPC and POPC lipids were taken from the previous studies (Berger et al., 1997). The atomic coordinates and the united atom parameters of the METH and DA were determined using the Automated Topology Builder (Malde et al., 2011; Stroet et al., 2018). Each simulated system consisted of 128 molecules of DPPC or POPC, which formed a bilayer among 10,628 simple point charge (SPC) water molecules (Berendsen et al., 1981).

At the initiation of simulation, a single molecule of ligand was randomly placed among the water molecules over the lipid membrane, and the ligand was fixed at a distance of about 4.5 nm above the center of mass (COM) of the lipid bilayer of each system. Following system energy minimization, MD simulation was conducted in the constant number of atoms, pressure, and temperature (NPT) ensemble for 1–2 μs with a 2-fs integration time step, using the Groningen Machine for Chemical Simulation (GROMACS) version 4.5.5 package (Abraham et al., 2015). The simulation was conducted at a temperature of 298 K using the velocity-rescale algorithm (Bussi et al., 2007) and controlled pressure by the Parrinello–Rahman algorithm (Parrinello and Rahman, 1981) at 1 bar with a time constant of 0.1 ps and a compressibility of 4.5 $\times$ 10-5 bar^{-1}. A cutoff of 1.0 nm was applied to the real-space part of electrostatic interactions and Lennard-Jones interactions. The long-range part of electrostatic interactions was calculated using the Ewald particle-mesh (Darden et al., 1993) with a 0.12 nm grid in the reciprocal space and cubic interpolation of 4. The LINCS algorithm was applied to constrain all bond lengths (Hess, 2008). The simulation protocol has been validated and used to study several biomolecular interactions, such as lipid-cholesterol interactions (Boonnoy et al., 2021; Enkavi et al., 2019), drug-membrane interactions (Khuntawee et al., 2021), nanoparticle-matrix interactions (Khuntawee et al., 2019; Nalakarn et al., 2019; Nisoh et al., 2020), membrane transport (Wong-Ekkabut and Karttunen, 2016), and protein-DNA interactions (Kongsema et al., 2019). The molecular visualization was created by the Visual Molecular Dynamics (VMD) software (Humphrey et al., 1996).

2.2. The hydrogen bond formation and lifetime calculation

The number of hydrogen bonds (H-bonds) between METH and DA molecules, and the components of lipid head groups (phosphate and glycerol-estermoieties) were calculated using the usual geometric restrictions for hydrogen bonding. A hydrogen bond is defined by the distance between the donor and the acceptor (rHB) $<$ 0.35 nm and the deviation from the linearity $<30^\circ$. The distance value of 0.35 nm corresponds to the first minimum of the radial distribution function (RDF) of water. Additionally, the average H-bond lifetime (τ) were calculated from the integration of the autocorrelation functions $C(t)$, calculated from the H-bond lifetime distribution (P(τ) (Boonnoy et al., 2024) as shown in the following formulas.

$$C(t) = 1 - \int_0^1 P(\tau)d\tau,$$

$$\tau = \int_0^\infty C(t)d\tau$$

2.3. Analysis of lipid bilayer properties

The structural and dynamic properties of the lipid bilayers were characterized by analyzing the unbiased molecular dynamics trajectories. All these parameters were calculated from the molecular dynamics trajectories using standard analysis tools from the GROMACS software (Abraham et al., 2015) suite. The custom Python scripts were used to average over the final 300 ns of each simulation to ensure that the system was at equilibrium. The following parameters were calculated to assess the effects of METH and DA on the bilayer properties. Deuterium order parameter (S_{CD}) was used to calculate the orientation order and motion of freedom of each hydrocarbon chain (sn-1 and sn-2) in the lipid bilayer of all simulation systems. The S_{CD} was determined using the prompt “gmx order” (Bartoš et al., 2025). Furthermore, the area per lipid (APL) represented the average surface area occupied by a single lipid molecule in the plane of the membrane. APL was calculated using the following equation:

$$APL = \frac{L_x \times L_y}{N_{lipids}}$$

where L_x and L_y are the average lengths of the simulation box vectors in the lateral plane. N_{lipids} is the total number of lipids in a single leaflet of the bilayer (Venable et al., 2015). Bilayer thickness(t) was calculated as the average distance between the phosphorus atoms of the lipid headgroups in the two opposing leaflets of the membrane (Gapsys et al., 2013). Volume per lipid (VPL) provides a three-dimensional measure of molecular packing and was determined by dividing the total volume of the simulation box by the total number of lipid molecules using the following equation:

$$VPL = \frac{L_x \times L_y \times L_z}{N_{lipids}}$$

where L_x, L_y, and L_z are the average lengths of the simulation box vectors, and N_{lipid} is the total number of lipid molecules in the system.

2.4. The potential of mean force (PMF) calculation

The potential of mean force (free energy) profiles for a METH or DA molecule partitioning across the DPPC and POPC lipid bilayers were determined by the biased umbrella-sampling MD simulations (Torrie and Valleau, 1977) with the Weighted Histogram Analysis Method (Kumar et al., 1992). The ligand (METH or DA) molecule was restrained to the center of mass (COM) of the lipid bilayer. A force constant of 1500 kJ mol^{-1} nm^{-2} was used for biasing potential in the Z-direction. The distance along the z-axis between the COMs of the ligand molecule and the bilayer's center varied from 0 to 4.5 nm with a 0.1 nm interval (a total of 46 simulation windows). All systems were performed under the constant number of atoms, volume, and temperature (NVT) ensemble at a temperature of 298 K. Each window was run for 100 ns, and the trajectories of the last 30 ns were extracted for free energy calculation. Statistical errors were estimated by the bootstrap analysis (Hub et al., 2010).

2.5. Cell cultures

Human neuroblastoma (SH-SY5Y) and human embryonic kidney (HEK 293T) cells were purchased from American Type Culture Collection (ATCC) (Manassas, VA, USA) and cultured in cell culture flasks (Corning Inc., Corning, NY, USA) with complete growth medium containing 1:1 mixture of Dulbecco's Modified Eagle Medium (DMEM) and F12 (Nutrient Mixture F-12(Ham's)), 10 % of inactivated fetal bovine serum (FBS) and 100 U/mL of penicillin/streptomycin. The cells were grown in a humidified incubator at 37 °C, 5 % CO_2, and 95 % humidity.

2.6. Cell treatment and cell viability assay

The cells were trypsinized using 0.25 % trypsin-EDTA (Gibco BRL, Gaithersburg, MD, USA) and resuspended in complete medium. The cells were seeded at a density of 1×10^4 cells per well in 96-well plates and grown in a humidified incubator for 24 h. Afterwards, the existing medium of each well from both cells was replaced with 0 (control), 0.5, 1, 1.5, and 2 mM of methamphetamine hydrochloride solution (purity >98.5 % using HPLC) (Lipomed AG, AMP-732-HC-100, Arlesheim, Switzerland), which was dissolved in serum-free medium for 24 h. Then, cell viability was evaluated by adding 150 μL of phosphate-buffered saline (PBS) containing 0.5 mg/ml of 3-(4,5-dimethylthiazol-2-yl)-2, 5-diphenyltetrozolium bromide (MTT) (Sigma-Aldrich, St. Louis, MO, USA) and incubating for 4 h in a humidified incubator at 37 °C. After the incubation, the MTT solution was gently aspirated. The formazan crystals were dissolved with 100 μL of dimethyl sulfoxide (DMSO) for 15 min at 37 °C on an orbital shaker before evaluating the optical density (OD) of formazan solution at 570 nm with 650 nm reference wavelength using the microplate reader (EZRead, 2000; Biochrom, UK).

2.7. Mitochondrial membrane potential assay

The mitochondrial membrane potential of cells was evaluated using Muse® Mitopotential Kit (Luminex, MCH100110, USA) and analyzed with Guava® Muse cell analyzer. The assay was performed following the manufacturer's protocol. In brief, the cells were seeded at a density of 3×10^5 cells per well in 6-well plates in a humidified incubator for 24 h. The following day, the cells were treated with 1 mM METH or serum-free medium and incubated in a humidified incubator at 37 °C for 24 h. Subsequently, the cells were trypsinized with 0.25 % trypsin-EDTA, centrifuged, and resuspended in 1X Assay buffer at a concentration of 1×10^5 cells/mL. The 100 μL of cell suspensions were mixed thoroughly with 95 μL of MitoPotential working solution (1:1000 of Muse® MitoPotential Dye and 1X Assay buffer). Then, the reaction was incubated for 20 min at 37 °C before adding 5 μL of Muse® MitoPotential 7-AAD reagent. The samples were incubated for an additional 5 min at room temperature. Finally, MitoPotential was detected using the Guava® Muse cell analyzer. The scatter plots of mitochondrial membrane potential representing cell viability and percentage of live/dead/depolarized cells were obtained and used for further statistical analysis.

2.8. Western blot analysis

Cell suspension samples from each experimental group were centrifuged, and the cell pellets were collected. The cell pellet was resuspended and lysed in RIPA buffer (50 mM Tris-HCl pH 7.4, 150 mM NaCl, 1 mM EDTA, 1 % Triton X-100, 1 % sodium deoxycholate, 0.1 % SDS, and 1 % protease inhibitor), then homogenized and centrifuged at 4 °C, 12,000 g for 15 min. Following that, the supernatant was collected to determine protein concentration using the Bradford technique (Bradford, 1976). Then, samples with similar total protein concentrations from each experimental condition were prepared using sample buffer (62.5 mM Tris-HCl, pH 6.8, 2 % SDS, 10 % glycerol, 2 % mercaptoethanol, and 0.01 % bromophenol blue). These samples were then denatured at 95 °C for 10 min. The denatured samples, a protein molecular weight marker (BlueEyed, PS-104, Jena Bioscience), and Precision Plus Protein Western C Blotting Standards (1610376, Bio-Rad) were then loaded into an SDS-PAGE gel for electrophoresis. Proteins isolated by electrophoresis were transferred onto polyvinylidene difluoride (PVDF) membranes (GE Healthcare Life Science, USA). The membranes were blocked for 1 h at room temperature with 5 % nonfat milk in Tris-buffered saline containing 0.1 % Tween-20 (TBS-T), followed by overnight incubation with primary antibodies at 4 °C. The primary antibodies included rabbit monoclonal anti-dopamine transporter (1:1000, AB184451, Abcam) and mouse monoclonal anti-actin (1:5000, MAB1501, Merk Millipore). The following day, membranes were incubated with a horseradish-conjugated anti-rabbit (1:2500, 7074, Cell Signaling Technology) or anti-mouse IgG (1:10000, 7076, Cell Signaling Technology) together with Anti-biotin, HRP-linked Antibody (1:10000, 7075P5, Cell Signaling Technology) for 60 min at room temperature. The signal of protein bands was enhanced using Clarity™ Western ECL Substrate (1705060, Bio-Rad) and detected by Vilber Fusion FX7 Image Analyzer. The density of immunoblot bands was analyzed with ImageJ software (National Institutes of Health, Bethesda, MD, USA). All protein densities were normalized to the expression of actin within their respective sample.

2.9. Data processing and statistical analysis

The results of an *in-silico* MD simulation were obtained using GROMACS and visualized with VMD. Moreover, the number of hydrogen bond formations was analyzed using the GROMACS package, based on data from the last 1 μs of unbiased simulation systems. For PMFs, the free energy of the last 30 ns of biased simulation was obtained and plotted using GraphPad Prism version 9 (Swift, 1997). For cell viability evaluation, the data from the MTT assay were analyzed using one-way ANOVA corrected by Dunnett's test for multiple comparisons between the control and each group of METH treated cells with different concentrations. Furthermore, the scatter plot and percentage of cells in all populations generated from mitochondrial membrane potential analysis were obtained. The statistical differences were calculated using an unpaired *t*-test to compare between control and METH treated group. The significant cut-off is at p-value <0.05.

3. Results

3.1. Properties of lipid bilayer of DPPC and POPC simulation systems

The structural and dynamic properties of the phospholipid bilayers were characterized by analyzing the deuterium order parameter (S_{CD}) for each carbon atom in the sn-1 and sn-2 acyl chains (Fig. 1A–D). The S_{CD} profiles of the DPPC systems (METH-DPPC and DA-DPPC) showed high and relatively flat ordering for both the sn-1 and sn-2 chains. The

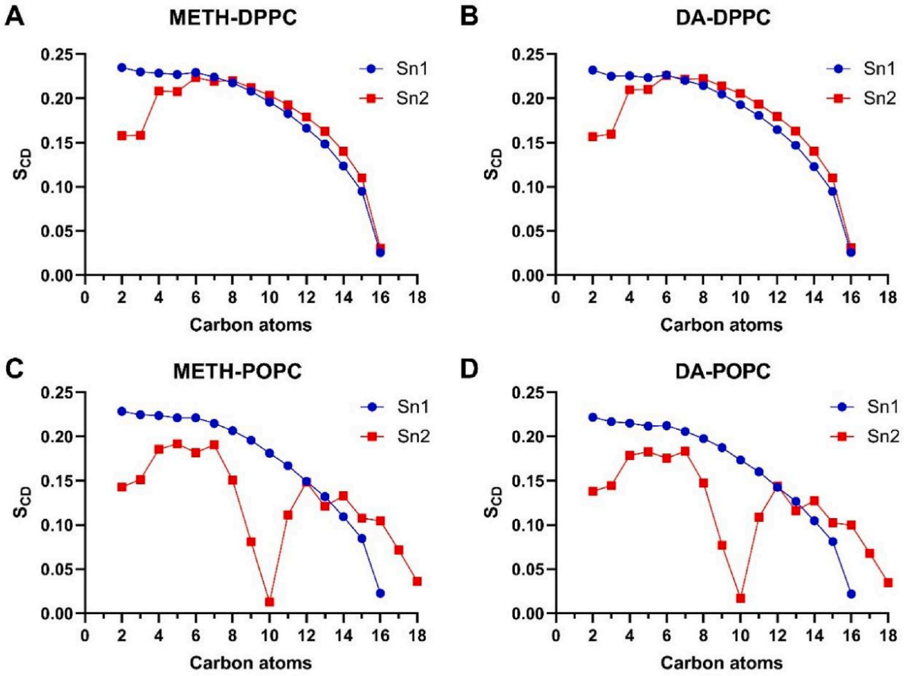

E

System	Area per lipid (APL) (nm^2)	Bilayer thickness (nm)	Volume per lipid (VPL) (nm^3)
METH-DPPC	0.615 ± 0.010	3.758 ± 0.054	1.156 ± 0.007
DA-DPPC	0.616 ± 0.013	3.742 ± 0.073	1.152 ± 0.008
METH-POPC	0.638 ± 0.008	3.775 ± 0.046	1.205 ± 0.007
DA-POPC	0.645 ± 0.011	3.732 ± 0.054	1.204 ± 0.007

Fig. 1. The deuterium order parameters (S_{CD}) of both acyl chains of phospholipid (Sn1 and Sn2) from 4 simulation systems including (A) METH-DPPC, (B) DA-DPPC, (C) METH-POPC and (D) DA-POPC. The other properties related to the phase of lipid bilayer of each system were demonstrated in Table-E, including Area per lipid (APL), Bilayer thickness and Volume per lipid (VPL). This data is shown as mean ± SD.

average S_{CD} value for these chains was approximately 0.17, reaching a peak of ~0.23 at the initial carbon atoms before gradually decreasing towards the terminal methyl groups. Meanwhile, the saturated sn-1 chain in POPC systems exhibited a profile similar to that of DPPC. Its ordering was slightly lower, with an average S_{CD} of ~0.16. The key finding was the behavior of the unsaturated sn-2 chain, which showed a sharp decrease in S_{CD} near the position of the double bond (C_9–C_{10}), with a value reaching a minimum of ~0.02. Furthermore, an analysis of key lipid bilayer parameters, including APL, bilayer thickness, and VPL, was depicted in Fig. 1E. The POPC systems exhibited a larger APL (~0.64 nm^2) compared to the DPPC systems (~0.61 nm^2). The bilayer thickness data showed that the DPPC bilayers (~3.75 nm) were thinner than the POPC bilayers by approximately 0.01 nm. Eventually, the VPL values were slightly higher for the POPC systems (~1.20 nm^3) than the DPPC systems (~1.15 nm^3). Across all parameters, no statistically significant differences were observed between the METH and DA systems for a given lipid type.

3.2. Translocation of METH and dopamine through DPPC and POPC phospholipid bilayers using unbiased simulation

To study the permeation of METH and DA molecules into the lipid bilayer, the initial positions of the ligand molecules were set in the water phase at a distance of 4.5 nm from the bilayer center to avoid the bias of the interactions between the molecules and the lipid bilayer. This setup allowed the ligand molecule to move and rotate freely in aqueous solution before approaching the bilayer surface. The distance in the z-axis of the molecule away from the lipid bilayer's center was determined as a function of time. The results of 4 unbiased MD simulations, METH-DPPC, METH-POPC, DA-DPPC, and DA-POPC, are illustrated in Fig. 2. METH and DA in the aqueous phase spontaneously moved toward the lipid bilayer and approached the bilayer surface. For the METH-DPPC and METH-POPC systems, the METH molecule attached to the bilayer with the aromatic ring and readily permeated into the lipid bilayer within approximately 10 ns? The METH remained within the bilayer for the rest of the simulation time. In addition, METH could freely move in the fatty acid tail of the membrane and frequently flip-flop between lipid leaflets. Interestingly, METH in the DPPC bilayer exhibits a higher flip-flop rate than in the POPC bilayer, but it tends to spend more time interacting with the carbonyl layer in the POPC system. For the DA-DPPC and DA-POPC systems, the DA molecule initially approached the bilayer surface but did not permeate into the bilayer over a thousand nanoseconds, as illustrated in Fig. 2C and D. After DA approached the bilayer interface for 500 ns in DPPC and 800 ns in POPC lipid bilayer, DA could not deeply penetrate and remained underneath the phosphate group for the rest of the simulation.

3.3. H-bond formation between ligands and hydrophilic head of the phospholipid bilayer

The number of H-bond formation between ligands, METH and DA, and the phospholipid bilayers (DPPC and POPC) were determined in Table 1. The result showed that METH formed a small number of hydrogen bonds with phosphate groups and carbonyl groups in both lipid systems. The number of H-bond formations with Phosphate groups and Carbonyl groups is less than 1 and 0.01, respectively. In contrast, DA exhibited a higher number of H-bond formations with the phosphate group (approximately 2 bonds), but a lesser number with carbonyl groups, similar to METH. The result of H-bond lifetime distribution showed that DA is stronger in forming H-bonds with Phosphate groups

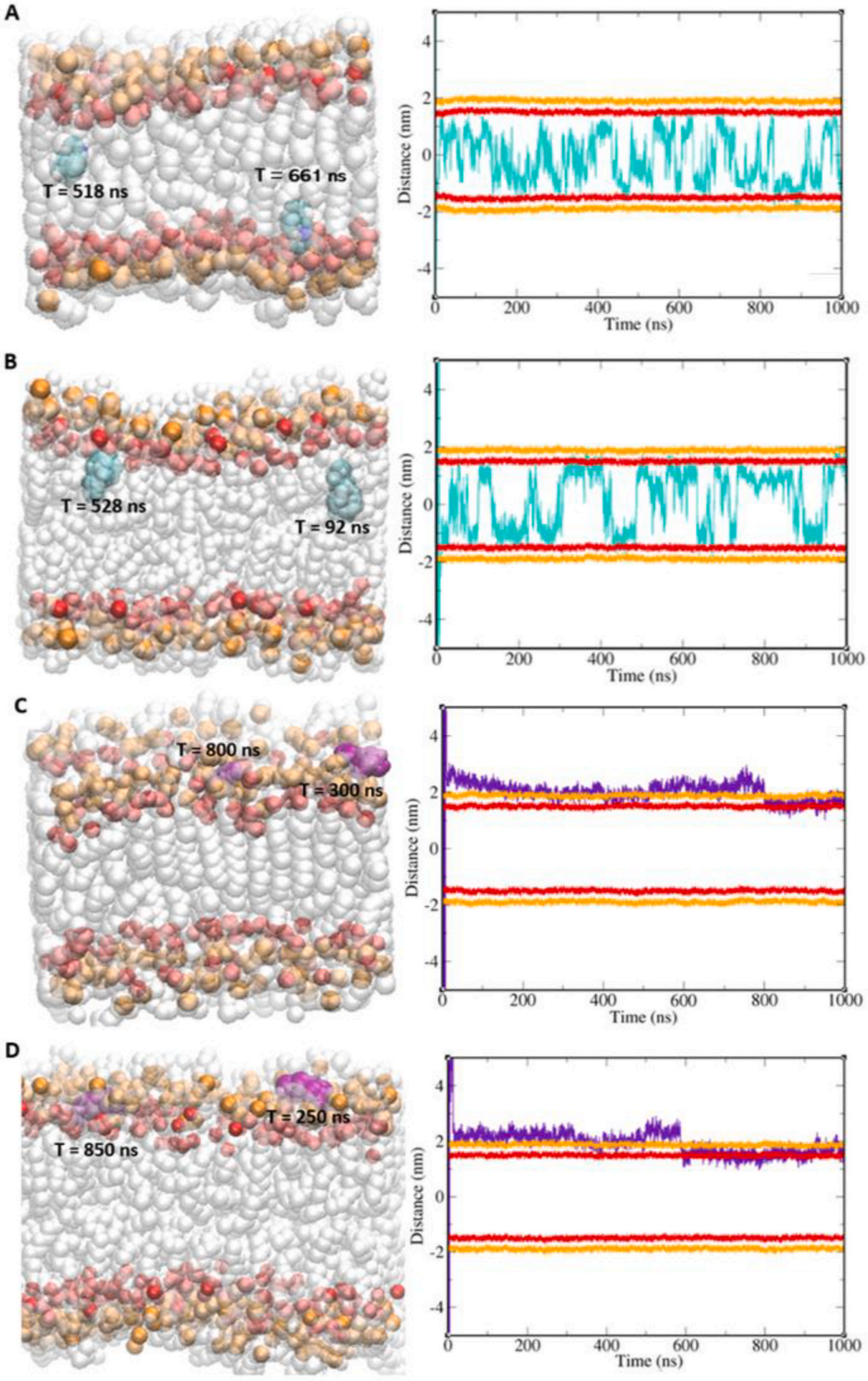

Fig. 2. The translocation of METH and DA into phospholipid bilayers. The simulations were performed including **(A)** the METH ligand in DPPC lipid membrane, **(B)** the METH ligand in POPC lipid membrane, **(C)** the DA ligand in DPPC lipid membrane and **(D)** the DA ligand in POPC lipid membrane. All figures show a Snapshot of lipid bilayer simulation and the location of target molecules in different simulation times (left), and the graph shows the location of target molecules during the simulation period. Each type of molecule was illustrated and discriminated by different colors as follows: Cyan (METH), Purple (DA), Orange (Phosphate groups), Red (Carbonyl groups) and Pale grey (Fatty acid). (For interpretation of the references to color in this figure legend, the reader is referred to the Web version of this article.)

than METH, with the H-bond lifetimes of 40 and 150 ns for DPPC and POPC, respectively. In contrast, both METH and DA form fewer H-bonds with the carbonyl group, with an H-bond lifetime of 0.20 ns? The strong hydrogen bonds binding between DA and phosphate groups indicated that the translocation of DA deeply into the hydrophobic region of the lipid bilayer is unfavorable.

3.4. Potential of mean force profile of METH and DA translocation into lipid bilayers

The potential of mean force (PMF) profiles was calculated to quantitatively describe the free energy changes associated with the translocation of a single molecule of methamphetamine (METH) or dopamine

Table 1
The average number of hydrogen bonding formations between the ligand of each system with phosphate groups and carbonyl groups of the lipid membrane.

System	Average no. of H-bond (bonds)		H-bond lifetime (ns)	
	Phosphate groups	Carbonyl groups	Phosphate groups	Carbonyl groups
METH-DPPC	0.07 ± 0.26	0.08 ± 0.27	0.04	0.04
METH-POPC	0.26 ± 0.44	0.06 ± 0.24	0.11	0.04
DA-DPPC	2.08 ± 0.39	0.02 ± 0.13	155.89	0.19
DA-POPC	2.10 ± 0.43	0.02 ± 0.14	41.56	0.01

This data is shown as mean ± SD.

(DA) across DPPC and POPC lipid bilayers (Fig. 3). The free energy profiles revealed distinct and characteristic behaviors for the two ligands. In the case of dopamine (DA), both the DPPC and POPC systems exhibited a decrease in free energy as the molecule moved from the bulk solvent toward the lipid-water interface (Z = 3.5 nm). A free energy minimum of approximately −23 kJ/mol was observed in the headgroup region at Z = 1 nm. This minimum represents a favorable binding site at the membrane interface. However, further penetration into the hydrophobic core resulted in a sharp increase in free energy with a significant energy barrier of approximately +10 kJ/mol at the bilayer's center (Z = 0 nm). This positive free energy indicates that the full translocation of DA into the hydrophobic core is an unfavorable process. In contrast, the PMF profiles for METH demonstrate a very different energy landscape. The free energy exhibits a substantial decrease as METH approaches the bilayer, reaching a deep free energy minimum in the acyl chain region. The minimum was observed at approximately −45 kJ/mol at Z = 2.0 nm and −42 kJ/mol at Z = 2.2 nm for the POPC and DPPC system, respectively. Crucially, the free energy does not rise to a positive value but remains in a negative value, plateau of approximately −20 to −25 kJ/mol, indicating that the hydrophobic core represents a favorable location for METH. Moreover, the lower free energy minimum observed for METH in the POPC bilayer indicates a more favorable partitioning into the unsaturated membrane.

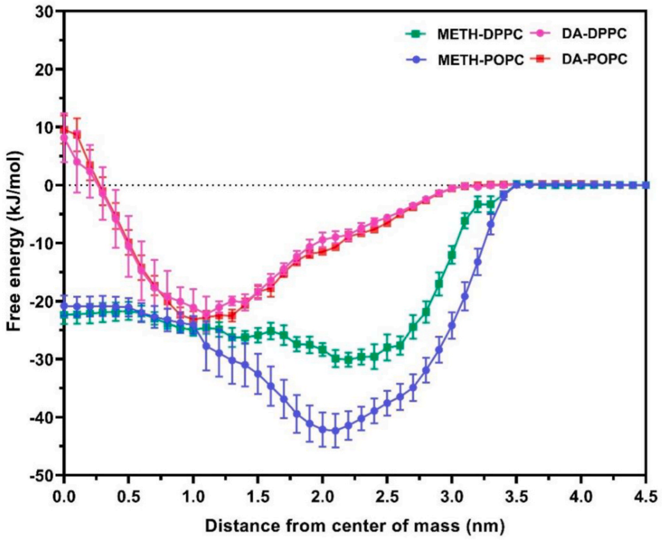

Fig. 3. The potential of mean force (PMF) profile shows the average free energy of a single molecule of each ligand when pulled toward the center of the lipid bilayer at an initial distance of 4.5 nm from the center of mass. The graph shows the energy profile of system METH-POPC (blue), METH-DPPC (green), DA-DPPC (pink), and DA-POPC (red). The data are shown as mean ± SEM of free energy for the last 30 ns of each individual experiment. (For interpretation of the references to color in this figure legend, the reader is referred to the Web version of this article.)

3.5. Dose-dependent effects of METH toxicity caused cell death in DAT-expressing and non-DAT-expressing cells

Fig. 4A displays a western blot analysis to demonstrate the expression of dopamine transporter protein (DAT) in SH-SY5Y and HEK293T cells. In this experiment, the rat striatum (STA) was used as a positive control for DAT expression to assess the efficacy of the experimental protocol for detecting DAT. The results showed that DAT was detected only in protein extracts from STA and SH-SY5Y cells, but not in proteins from HEK293T cells. After determining DAT expression, the cell viability of both cell lines was determined using MTT assays. As shown in Fig. 4B–C, METH can induce a reduction in cell viability in a dose-dependent manner from 0.5 mM to 2.0 mM in both cell lines. METH exposure to HEK293T cells at 0.5–2.0 mM significantly decreased cell viability ($P < 0.0001$) compared to control-untreated cells. METH significantly decreased cell viability in SH-SY5Y cells at 1.0 mM ($P < 0.05$), 2.5 mM ($P < 0.01$), and 2 mM ($P < 0.001$) compared to control-untreated cells, respectively.

3.6. METH affects mitochondrial membrane potential and cell viability on both DAT-expressing and non-DAT-expressing cells

The mitochondrial membrane potential assay kit was used to measure changes in mitochondrial membrane potential caused by METH treatment. This assay could reveal whether METH treatment could cause a toxic effect on mitochondria in both DAT-expressing cells and non-DAT-expressing cells, leading to cell death. The dots in scatter plots reflect each cell allocated to a population based on its status. As shown in Figs. 5 and 6, the METH treatment depolarized the mitochondrial membrane and induced cell death in both cell types, as indicated by a greater number of dots shifting from the live (lower right) zone to the depolarized/dead (upper left) zone compared to the control group. The percentage of each cell population shown in Fig. 5B illustrates that the percentage of live cells in SH-SY5Y and HEK293T was significantly decreased ($P < 0.001$ and $P < 0.01$) after METH treatment. In contrast, the percentage of dead cells in both cell types significantly increased ($P < 0.05$ and $P < 0.0001$) compared to control-untreated cells. METH exposure significantly increased the percentage of depolarized live cells in SH-SY5Y and HEK293T ($P < 0.01$ and $P < 0.001$) compared to control. Both cell types demonstrated a significant increase in depolarized dead cells ($P < 0.05$) and total dead cells ($P < 0.05$) compared to control cells, respectively.

4. Discussion

The current study provides novel evidence to support the process by which METH penetrates the mitochondrial membrane and disrupts its function via *in silico* and *in vitro* experimental models. METH spontaneously moved into both DPPC and POPC membranes, which are abundant phospholipid types of the cellular and mitochondrial membranes (Horvath and Daum, 2013).

In this study, MD simulation systems of both POPC and DPPC lipid bilayers were set at room temperature (298K), which theoretically affects the phase of the POPC bilayer as liquid-crystalline (Wanderlingh et al., 2017) and DPPC bilayer as a gel-like phase (Costa et al., 2024). However, the key findings from analysis of lipid bilayer properties of S_{CD}, APL, membrane thickness, and VPL illustrated that the presence of METH and DA profoundly altered the structure of the DPPC bilayer. As can be seen in the results of the lipid profile that the S_{CD} value of DPPC was a close value to the previous study, which performed a simulation of DPPC at 323K, which theoretically causes DPPC to be in the liquid phase (Klauda et al., 2010). Furthermore, in the pure DPPC bilayer in the gel phase at 298 K, one would expect a low APL (<0.45 nm^2), high S_{CD} (>0.3), and a thick bilayer (>4.0 nm)(Drabik et al., 2020). Interestingly, the introduction of METH and DA caused a significant fluidization of the membrane. This is evidenced by a substantial increase in APL (~0.61

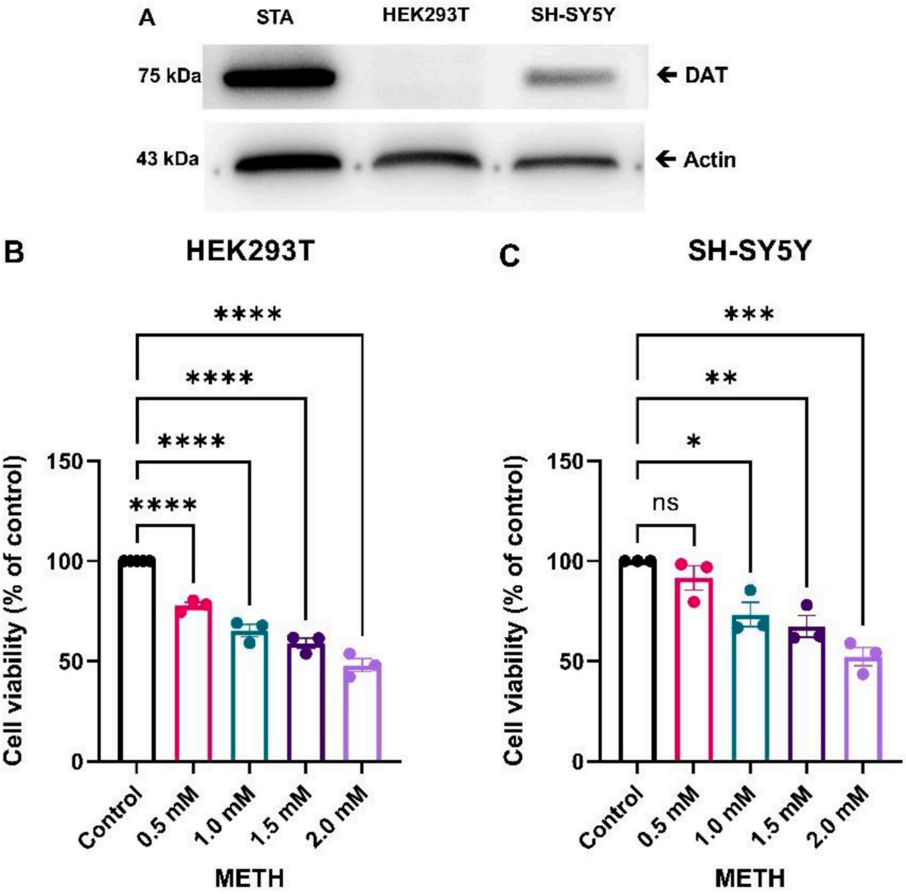

Fig. 4. **(A)** The western blot analysis of dopamine transporter (DAT) in the striatum (STA) of rat brain, HEK293T cells, and SH-SY5Y cells. **(B–C)** The graph shows cell viability of HEK293T cells and SH-SY5Y cells after 1 h treatment with different concentrations of METH. The results are shown by mean ± SEM of 3 independent experiments. $^{*}P < 0.05$, $^{**}P < 0.01$, $^{***}P < 0.001$ and $^{****}P < 0.0001$ compared to control.

nm^2), a decrease in S_{CD} (~0.17), and a marked reduction in bilayer thickness (~3.75 nm). These values indicate that the DPPC bilayer, under the influence of the drugs, exists in a disordered gel-like state, with properties converging toward those of the fluid POPC bilayer. Additionally, the DPPC and POPC bilayer systems in this study showed APL and thickness values similar to those from simulations of complex mitochondrial membranes (Mai et al., 2023). Our APL values (~0.61 nm^2 for DPPC and ~0.64 nm^2 for POPC) fall within the reported range for mitochondrial membranes (~60–63 Å^2). Although the bilayer thickness (~3.75 nm) is slightly less than that of mitochondrial models (~4.0 nm), this supports the biological relevance of our model and its ability to capture key features of real mitochondrial membranes.

Furthermore, the results from unbiased simulations, PMF profiles, and H-bond analysis elucidated the distinct behaviors of METH and DA regarding their translocation through lipid bilayers. The unbiased simulation trajectories demonstrated that METH freely penetrates both types of phospholipid bilayers and resides within the hydrophobic core, while DA primarily remains at the membrane-water interface. These behaviors are strongly supported by the PMF and H-bond formation data. METH has a low molecular weight and contains a major non-polar component (Zhang et al., 2020), exhibiting a deep free energy minimum in the hydrophobic core of both DPPC and POPC bilayers, indicating a thermodynamically favorable location. This is consistent with its low number of H-bonds and short bonding lifetime, which enables it to bypass the polar headgroup region and partition into the membrane. This behavior aligns with previous studies on small, uncharged molecules, such as Fullerenes (Nisoh et al., 2022) and Zinc sulfide nanoparticles (Kumar Basak et al., 2020), which have also been shown to permeate lipid membranes and freely locate in the hydrophobic tail region. In contrast, DA demonstrated a strong affinity for the membrane interface. It forms high-bonding formation and long-lasting hydrogen bonds with the phosphate groups of the phospholipids, a finding consistent with its strong polarity due to the presence of two hydroxyl groups (Zhou et al., 2017). This stable interaction with the headgroup region results in a low free energy minimum at the interface but also creates a significant energy barrier of approximately +10 kJ/mol for translocation into the hydrophobic core. By using DA as a reference molecule that has a low potential to permeate membranes and is less stable at the membrane core, we have demonstrated that METH behaves fundamentally differently, supporting the potential for METH to directly penetrate lipid membranes, such as those found in mitochondria.

Interestingly, when comparing the results from unbiased simulations of METH between DPPC and POPC systems, the distance graph shows that METH molecules tended to move across the upper and lower leaflets of the DPPC lipid bilayer with higher frequency than in the METH-POPC system. This event was supported by the PMF results that the free energy minimum for METH was deeper in the POPC bilayer (~-45 kJ/mol) compared to the DPPC bilayer (~-42 kJ/mol). In addition, this event consists of a number of H-bonds and lifetime from the POPC system, which is slightly higher than the result of the DPPC system. These demonstrate a more thermodynamically favorable partitioning for METH in the unsaturated membrane. Therefore, the structural difference of DPPC may drive this behavior of METH, as DPPC is composed of two saturated acyl chains. In contrast, POPC has one unsaturated acyl chain combined with another saturated chain as its hydrophobic tails (Angladon et al., 2019). Consequently, this structural difference affects the environment in the hydrophobic section of the bilayer, as DPPC contains a higher density and more uniform environment than POPC,

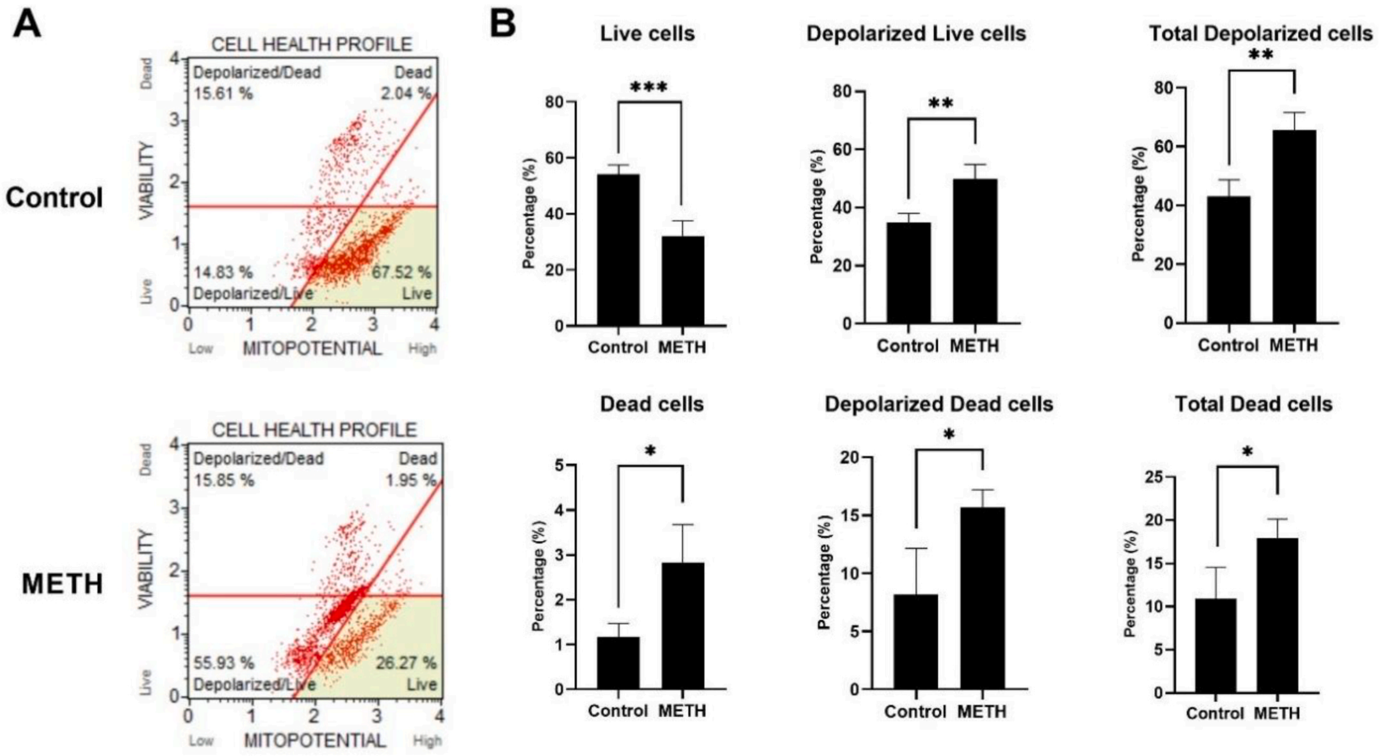

Fig. 5. The mitochondrial membrane potential and cell death assay in DAT-expressing cell (SH-SY5Y). **(A)** The scatterplot of Control and METH group. **(B)** The comparison of cell population in each scatterplot area to evaluate mitochondrial membrane potential in live and dead cells after being treated with 1 mM of METH for 1 h. The data are expressed as mean ± SEM of 4 independent experiments. $^*P < 0.05$, $^{**}P < 0.01$ and $^{***}P < 0.001$ compared to control.

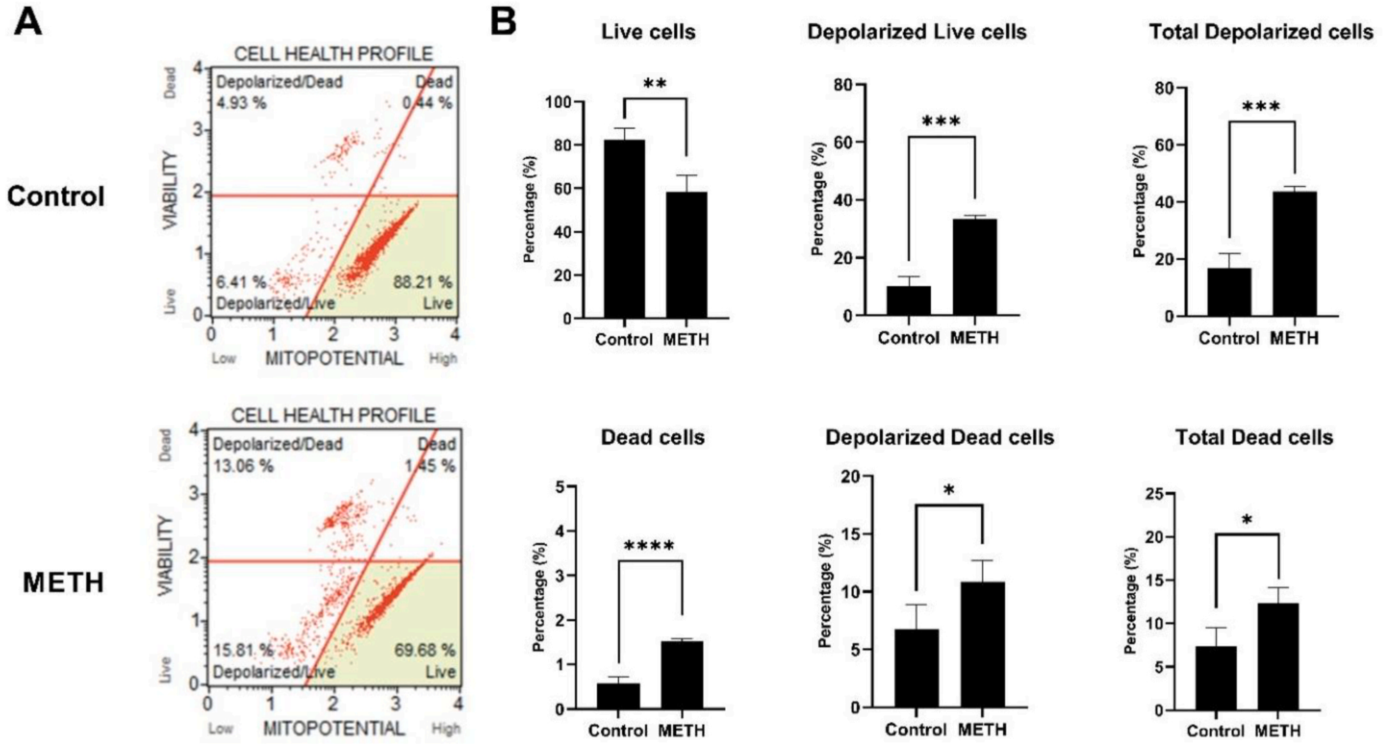

Fig. 6. The mitochondrial membrane potential and cell death assay in non-DAT-expressing cell (HEK293T). **(A)** The scatterplot of Control and METH group. **(B)** The comparison of cell population in each scatterplot area to evaluate mitochondrial membrane potential in live and dead cells after being treated with 1 mM of METH for 1 h. The data are expressed as mean ± SEM of 4 independent experiments. $^*P < 0.05$, $^{**}P < 0.01$, $^{***}P < 0.001$ and $^{****}P < 0.0001$ compared to control.

which has a looser and more irregular environment in the hydrophobic layer (Pinisetty et al., 2006). Hence, METH molecules more easily navigated the high density of non-polar molecules due to its major structural compartment being a nonpolar molecule (Zhang et al., 2020). Additionally, the number of bonds that METH forms with the phosphate group of the POPC system is slightly higher than that of the DPPC system due to the stronger polarity of the phosphate group of the POPC lipid (Marsh, 2001).

Several studies have investigated the upstream effects of METH-induced mitochondrial dysfunction, focusing on its ability to bind to and pass through the DAT on neuronal membranes (Hedges et al., 2018). The administration of METH is known to alter the function of DAT and VMAT, causing reversal and subsequent increased DA levels in the presynaptic sites and synaptic cleft (Verónica et al., 2001). The degradation of high amounts of freed DA results in the generation of ROS that could damage various cellular compartments, including mitochondria, causing mitochondrial dysfunction (Jang et al., 2017). Furthermore, previous studies from our group have also demonstrated that METH treatment induces neurotoxic mechanisms related to mitochondrial dysfunction, leading to degeneration in the striatum, hippocampus, and prefrontal cortex of rats (Kraiwattanapirom et al., 2021; Polvat et al., 2023). Together, this past research could support the theoretical DAT-dependent pathway of METH induced cell death via alteration of mitochondrial function. In addition, this DAT-dependent pathway of METH induced mitochondrial dysfunction is supported by previous research demonstrating that blockage of DAT attenuated the neurotoxic effect of METH on mitochondria (Tunstall et al., 2018). Notably, the present study can extend our understanding of the neurotoxic mechanisms of METH on mitochondrial function. The results of the cell culture study suggest that HEK293T cells, which are non-DAT-expressing cells, can be damaged by a cytotoxic effect caused by METH treatment, as it increased mitochondrial depolarization and cell death, which was also observed in SH-SY5Y-DAT-expressing cells. This finding highlights the potential of METH induced mitochondrial dysfunction to occur via a DAT-independent process. This DAT-independent mechanism is also supported by previous research using other cells lacking DAT, such as mesenchymal stem cells (MSCs) (Gaggi et al., 2020; Y. Shen et al., 2018) and glial cells (D'Brant et al., 2019; Lau et al., 2000; Sharikova et al., 2018). In MSC cells, METH treatment disrupted several key indices of mitochondrial function, including mitochondrial membrane potential, mitochondrial dynamics, ATP production, and mitochondrial biogenesis, ultimately leading to mitochondrial hyperfragmentation and cell death (Yulai Shen et al., 2018). Similarly, in neural glial cells, the toxic effect of METH treatment was measured by the disturbance of mitochondrial function. For instance, a study using C6 astroglioma cell culture showed a reduction of mitochondrial volume and increased apoptosis after METH treatment (D'Brant et al., 2019). Furthermore, in human astrocyte cell cultures, METH treatment induced a change in mitochondrial membrane potential and increased ROS production. In addition, it has been proposed that the METH induced alteration of mitochondrial function might relate to ROS generation and decreased ATP production as underlying mechanisms to initiate apoptotic processes (Lau et al., 2000). Similarly, research using microglial cells has demonstrated that METH induces the activation of the mitochondrial-dependent intrinsic apoptosis pathway in microglia by reducing the mitochondrial respiratory process (Sharikova et al., 2018). This evidence suggests that the neurotoxic mechanism of METH is likely to be via a DAT-independent pathway.

It has been suggested that METH causes membrane depolarization due to its molecular structure, which contains a weak base property resulting from its amine composition. Once the METH reached the acidic environment, it could act as a proton acceptor and transform into an ionic form, which contained a +1 positive charge (Abbruscato and Trippier, 2018). This change in polarity might cause the pH gradient between intermembrane space and matrix to collapse, interfering with the membrane potential of mitochondria, which is a similar mechanism when METH disturbs VMAT function (Sulzer and Rayport, 1990). With METH causing mitochondrial depolarization in non-DAT expressing cells, this could result in interruption of the electron transport chain, decreasing ATP production, and increasing the generation of ROS (Zorova et al., 2018) producing an upstream mechanism to trigger the occurrence of cytotoxicity and apoptosis.

5. Conclusion

The findings from *in silico* and *in vitro* experiments in the present study suggest a possible mechanism by which METH treatment-induced neuronal cell death is partly mediated via a DAT-independent pathway. The results have demonstrated that METH molecules can directly penetrate mitochondrial membranes and cause depolarization, which initiates downstream mechanisms resulting in mitochondrial dysfunction and cell death.

CRediT authorship contribution statement

Tanthai Polvat: Writing – review & editing, Writing – original draft, Methodology, Investigation, Funding acquisition, Formal analysis, Data curation, Conceptualization. **Wasinee Khuntawee:** Writing – original draft, Visualization, Methodology, Formal analysis. **Tanya Prasertporn:** Methodology, Investigation. **Kornkanok Promthep:** Methodology, Investigation. **Nathanon Kerdkaen:** Methodology, Investigation. **Jiraporn Panmanee:** Methodology, Investigation, Formal analysis. **Pornkamon Nalakarn:** Writing – original draft, Methodology, Formal analysis. **Jirasak Wong-ekkabut:** Writing – review & editing, Validation, Supervision, Resources, Project administration, Funding acquisition, Data curation, Conceptualization. **Banthit Chetsawang:** Writing – review & editing, Supervision, Resources, Project administration, Methodology, Funding acquisition, Formal analysis, Data curation, Conceptualization.

Declaration of generative AI and AI-assisted technologies

The authors declare that no AI and AI-assisted technologies were used in generation of text and result in this study.

Funding

This study was supported by the Royal Golden Jubilee (RGJ)-Ph.D. program (Grant No. PHD/0063/2561) through the National Research Council of Thailand (NRCT), Thailand Research Fund (TRF) and Mahidol University to TP and BC, and National Research Council of Thailand (NRCT) and Mahidol University through grant number N42A650340 to BC. JW was supported by the National Science Research and Innovation fund (NSRF) via the Program Management Unit for Human Resources & Institutional Development Research and Innovation (PMUB) [Grant No. B42G670041].

Declaration of competing interest

The authors declare that they have no known competing financial interests or personal relationships that could have appeared to influence the work reported in this paper.

Acknowledgements

The computing facilities were provided by Computational Biomodelling Laboratory for Agricultural Science and Technology (CBLAST), Faculty of Science, Kasetsart University, Bangkok, Thailand. The image analyzer and research assistance were provided by Mahidol University-Frontier Research Facility (MU-FRF), Thailand.

Data availability

Data will be made available on request.

References

Abbruscato, T.J., Trippier, P.C., 2018. DARK classics in chemical neuroscience: methamphetamine. ACS Chem. Neurosci. 9 (10), 2373–2378. https://doi.org/10.1021/acschemneuro.8b00123.

Abraham, M.J., Murtola, T., Schulz, R., Páll, S., Smith, J.C., Hess, B., Lindahl, E., 2015. GROMACS: high performance molecular simulations through multi-level parallelism from laptops to supercomputers. SoftwareX 1–2, 19–25. https://doi.org/10.1016/j.softx.2015.06.001.

Angladon, M.A., Fossepre, M., Leherte, L., Vercauteren, D.P., 2019. Interaction of POPC, DPPC, and POPE with the mu opioid receptor: a coarse-grained molecular dynamics study. PLoS One 14 (3), e0213646. https://doi.org/10.1371/journal.pone.0213646.

Bartoš, L., Pajtinka, P., Vácha, R., 2025. Gorder: comprehensive tool for calculating lipid order parameters from molecular simulations. SoftwareX 31, 102254. https://doi.org/10.1016/j.softx.2025.102254.

Berendsen, H.J.C., Postma, J.P.M., van Gunsteren, W.F., Hermans, J., 1981. Interaction models for water in relation to protein hydration. In: Pullman, B. (Ed.), Intermolecular Forces: Proceedings of the Fourteenth Jerusalem Symposium on Quantum Chemistry and Biochemistry Held in Jerusalem, Israel, April 13–16, 1981. Springer, Netherlands, pp. 331–342. https://doi.org/10.1007/978-94-015-7658-1_21.

Berger, O., Edholm, O., Jähnig, F., 1997. Molecular dynamics simulations of a fluid bilayer of dipalmitoylphosphatidylcholine at full hydration, constant pressure, and constant temperature. Biophys. J. 72 (5), 2002–2013. https://doi.org/10.1016/s0006-3495(97)78845-3.

Boonnoy, P., Janlad, M., Bagheri, B., Dias, C., Karttunen, M., Wong-ekkabut, J., 2024. Cholesterol inhibits oxygen permeation through biological membranes: mechanism against double-bond peroxidation [10.1039/D4RA04846F]. RSC Adv. 14 (40), 29113–29121. https://doi.org/10.1039/D4RA04846F.

Boonnoy, P., Jarerattanachat, V., Karttunen, M., Wong-ekkabut, J., 2021. Role of cholesterol flip-flop in oxidized lipid bilayers. Biophys. J. 120 (20), 4525–4535. https://doi.org/10.1016/j.bpj.2021.08.036.

Bradford, M.M., 1976. A rapid and sensitive method for the quantitation of microgram quantities of protein utilizing the principle of protein-dye binding. Anal. Biochem. 72, 248–254. https://doi.org/10.1016/0003-2697(76)90527-3.

Bussi, G., Donadio, D., Parrinello, M., 2007. Canonical sampling through velocity rescaling. J. Chem. Phys. 126 (1), 014101. https://doi.org/10.1063/1.2408420.

Choudhary, R.C., Kuschner, C.E., Kazmi, J., McDevitt, L., Espin, B.B., Essaihi, M., Nishikimi, M., Becker, L.B., Kim, J., 2024. The role of phospholipid alterations in mitochondrial and brain dysfunction after cardiac arrest. Int. J. Mol. Sci. 25 (9). https://doi.org/10.3390/ijms25094645.

Costa, L.F., Germiniani, L.G.L., Franco, L.F.M., 2024. An analysis of the dipalmitoylphosphatidylcholine bilayer gel phases predicted with molecular dynamics simulations using force fields from the GROMOS family. Fluid Phase Equilib. 583, 114115. https://doi.org/10.1016/j.fluid.2024.114115.

D'Brant, L.Y., Desta, H., Khoo, T.C., Sharikova, A.V., Mahajan, S.D., Khmaladze, A., 2019. Methamphetamine-induced apoptosis in glial cells examined under marker-free imaging modalities. J. Biomed. Opt. 24 (4), 1–10. https://doi.org/10.1117/1.JBO.24.4.046503.

Darden, T., York, D., Pedersen, L., 1993. Particle mesh Ewald: an N·log(N) method for Ewald sums in large systems. J. Chem. Phys. 98 (12), 10089–10092. https://doi.org/10.1063/1.464397.

Davidson, C., Gow, A.J., Lee, T.H., Ellinwood, E.H., 2001. Methamphetamine neurotoxicity: necrotic and apoptotic mechanisms and relevance to human abuse and treatment. Brain Res. Rev. 36 (1), 1–22. https://doi.org/10.1016/s0165-0173(01)00054-6.

Drabik, D., Chodaczek, G., Kraszewski, S., Langner, M., 2020. Mechanical properties determination of DMPC, DPPC, DSPC, and HSPC solid-ordered bilayers. Langmuir 36 (14), 3826–3835. https://doi.org/10.1021/acs.langmuir.0c00475.

Enkavi, G., Javanainen, M., Kulig, W., Róg, T., Vattulainen, I., 2019. Multiscale simulations of biological membranes: the challenge to understand biological phenomena in a living substance. Chem. Rev. 119 (9), 5607–5774. https://doi.org/10.1021/acs.chemrev.8b00538.

Gaggi, G., Di Credico, A., Izzicupo, P., Alviano, F., Di Mauro, M., Di Baldassarre, A., Ghinassi, B., 2020. Human mesenchymal stromal cells unveil an unexpected differentiation potential toward the dopaminergic neuronal lineage. Int. J. Mol. Sci. 21 (18). https://doi.org/10.3390/ijms21186589.

Galluzzi, L., Brenner, C., Morselli, E., Touat, Z., Kroemer, G., 2008. Viral control of mitochondrial apoptosis. PLoS Pathog. 4 (5), e1000018. https://doi.org/10.1371/journal.ppat.1000018.

Gapsys, V., de Groot, B.L., Briones, R., 2013. Computational analysis of local membrane properties. J. Comput. Aided Mol. Des. 27 (10), 845–858. https://doi.org/10.1007/s10822-013-9684-0.

Hedges, D.M., Obray, J.D., Yorgason, J.T., Jang, E.Y., Weerasekara, V.K., Uys, J.D., Bellinger, F.P., Steffensen, S.C., 2018. Methamphetamine induces dopamine release in the nucleus accumbens through a sigma receptor-mediated pathway. Neuropsychopharmacology 43 (6), 1405–1414. https://doi.org/10.1038/npp.2017.291.

Hess, B., 2008. P-LINCS: a parallel linear constraint solver for molecular simulation. J. Chem. Theor. Comput. 4 (1), 116–122. https://doi.org/10.1021/ct700200b.

Horvath, S.E., Daum, G., 2013. Lipids of mitochondria. Prog. Lipid Res. 52 (4), 590–614. https://doi.org/10.1016/j.plipres.2013.07.002.

Hub, J.S., de Groot, B.L., van der Spoel, D., 2010. g_WHAM—a free weighted histogram analysis implementation including robust error and autocorrelation estimates. J. Chem. Theor. Comput. 6 (12), 3713–3720. https://doi.org/10.1021/ct100494z.

Humphrey, W., Dalke, A., Schulten, K., 1996. VMD: visual molecular dynamics. J. Mol. Graph. 14 (1), 33–38. https://doi.org/10.1016/0263-7855(96)00018-5.

Jang, E.Y., Yang, C.H., Hedges, D.M., Kim, S.P., Lee, J.Y., Ekins, T.G., Garcia, B.T., Kim, H.Y., Nelson, A.C., Kim, N.J., Steffensen, S.C., 2017. The role of reactive oxygen species in methamphetamine self-administration and dopamine release in the nucleus accumbens. Addict. Biol. 22 (5), 1304–1315. https://doi.org/10.1111/adb.12419.

Khuntawee, W., Amornloetwattana, R., Vongsangnak, W., Namdee, K., Yata, T., Karttunen, M., Wong-ekkabut, J., 2021. In silico and in vitro design of cordycepin encapsulation in liposomes for colon cancer treatment [10.1039/D1RA00038A]. RSC Adv. 11 (15), 8475–8484. https://doi.org/10.1039/D1RA00038A.

Khuntawee, W., Sutthibutpong, T., Phongphanphanee, S., Karttunen, M., Wong-ekkabut, J., 2019. Molecular dynamics study of natural rubber–fullerene composites: connecting microscopic properties to macroscopic behavior [10.1039/C9CP03155C]. Phys. Chem. Chem. Phys. 21 (35), 19403–19413. https://doi.org/10.1039/C9CP03155C.

Klauda, J.B., Venable, R.M., Freites, J.A., O'Connor, J.W., Tobias, D.J., Mondragon-Ramirez, C., Vorobyov, I., MacKerell Jr., A.D., Pastor, R.W., 2010. Update of the CHARMM All-Atom additive force field for lipids: validation on six lipid types. J. Phys. Chem. B 114 (23), 7830–7843. https://doi.org/10.1021/jp101759q.

Kongsema, M., Wongkhieo, S., Khongkow, M., Lam, E.W., Boonnoy, P., Vongsangnak, W., Wong-Ekkabut, J., 2019. Molecular mechanism of Forkhead box M1 inhibition by thiostrepton in breast cancer cells. Oncol. Rep. 42 (3), 953–962. https://doi.org/10.3892/or.2019.7225.

Kraiwattanapirom, N., Komlao, P., Harnpramukkul, A., Promyo, K., Ngampramuan, S., Chetsawang, B., 2021. The neuroprotective role of melatonin against methamphetamine toxicity-induced neurotransmission dysregulation and cognitive deficits in rats. Food Chem. Toxicol. 157, 112610. https://doi.org/10.1016/j.fct.2021.112610.

Kumar Basak, U., Roobala, C., Basu, J.K., Maiti, P.K., 2020. Size-dependent interaction of hydrophilic/hydrophobic ligand functionalized cationic and anionic nanoparticles with lipid bilayers. J. Phys. Condens. Matter 32 (10), 104003. https://doi.org/10.1088/1361-648X/ab5770.

Kumar, S., Rosenberg, J.M., Bouzida, D., Swendsen, R.H., Kollman, P.A., 1992. THE weighted histogram analysis method for free-energy calculations on biomolecules. I. The method. J. Comput. Chem. 13 (8), 1011–1021. https://doi.org/10.1002/jcc.540130812.

Kuschner, C.E., Choi, J., Yin, T., Shinozaki, K., Becker, L.B., Lampe, J.W., Kim, J., 2018. Comparing phospholipid profiles of mitochondria and whole tissue: higher PUFA content in mitochondria is driven by increased phosphatidylcholine unsaturation. J. Chromatogr., B: Anal. Technol. Biomed. Life Sci. 1093–1094, 147–157. https://doi.org/10.1016/j.jchromb.2018.07.006.

Lau, J.W., Senok, S., Stadlin, A., 2000. Methamphetamine-induced oxidative stress in cultured mouse astrocytes. Ann. N. Y. Acad. Sci. 914, 146–156. https://doi.org/10.1111/j.1749-6632.2000.tb05192.x.

Mai, T.L., Derreumaux, P., Nguyen, P.H., 2023. Structure and elasticity of mitochondrial membranes: a molecular dynamics simulation Study. J. Phys. Chem. B 127 (50), 10778–10791. https://doi.org/10.1021/acs.jpcb.3c05112. Epub 2023 Dec 12.

Malde, A.K., Zuo, L., Breeze, M., Stroet, M., Poger, D., Nair, P.C., Oostenbrink, C., Mark, A.E., 2011. An automated force field topology builder (ATB) and repository: version 1.0. J. Chem. Theor. Comput. 7 (12), 4026–4037. https://doi.org/10.1021/ct200196m.

Marsh, D., 2001. Polarity and permeation profiles in lipid membranes. Proc. Natl. Acad. Sci. 98 (14), 7777–7782. https://doi.org/10.1073/pnas.131023798.

Nalakarn, P., Boonnoy, P., Nisoh, N., Karttunen, M., Wong-ekkabut, J., 2019. Dependence of fullerene aggregation on lipid saturation due to a balance between entropy and enthalpy. Sci. Rep. 9 (1), 1037. https://doi.org/10.1038/s41598-018-37659-4.

Nisoh, N., Jarerattanachat, V., Karttunen, M., Wong-Ekkabut, J., 2020. Formation of aggregates, icosahedral structures and percolation clusters of fullerenes in lipids bilayers: the key role of lipid saturation. Biochim. Biophys. Acta Biomembr. 1862 (9), 183328. https://doi.org/10.1016/j.bbamem.2020.183328.

Nisoh, N., Jarerattanachat, V., Karttunen, M., Wong-ekkabut, J., 2022. Fullerenes' interactions with plasma membranes: insight from the MD simulations. Biomolecules 12 (5), 639. https://www.mdpi.com/2218-273X/12/5/639.

Nordahl, T.E., Salo, R., Leamon, M., 2003. Neuropsychological effects of chronic methamphetamine use on neurotransmitters and cognition: a review. J. Neuropsychiatry Clin. Neurosci. 15 (3), 317–325. https://doi.org/10.1176/jnp.15.3.317.

Parrinello, M., Rahman, A., 1981. Polymorphic transitions in single crystals: a new molecular dynamics method. J. Appl. Phys. 52 (12), 7182–7190. https://doi.org/10.1063/1.328693.

Pinisetty, D., Moldovan, D., Devireddy, R., 2006. The effect of methanol on lipid bilayers: an atomistic investigation. Ann. Biomed. Eng. 34 (9), 1442–1451. https://doi.org/10.1007/s10439-006-9148-y.

Polvat, T., Prasertporn, T., Na Nakorn, P., Pannengpetch, S., Suwanjang, W., Panmanee, J., Ngampramuan, S., Cornish, J.L., Chetsawang, B., 2023. Proteomic analysis reveals the neurotoxic effects of chronic methamphetamine self-administration-induced cognitive impairments and the role of melatonin-enhanced restorative process during methamphetamine withdrawal. J. Proteome Res. 22 (10), 3348–3359. https://doi.org/10.1021/acs.jproteome.3c00502.

Sharikova, A.V., Quaye, E., Park, J.Y., Maloney, M.C., Desta, H., Thiyagarajan, R., Seldeen, K.L., Parikh, N.U., Sandhu, P., Khmaladze, A., Troen, B.R., Schwartz, S.A., Mahajan, S.D., 2018. Methamphetamine induces apoptosis of microglia via the intrinsic mitochondrial-dependent pathway. J. Neuroimmune Pharmacol. 13 (3), 396–411. https://doi.org/10.1007/s11481-018-9787-4.

Shen, Y., Wu, L., Wang, J., Wu, X., Zhang, X., 2018. The role of mitochondria in methamphetamine-induced inhibitory effects on osteogenesis of mesenchymal stem cells. Eur. J. Pharmacol. 826, 56–65. https://doi.org/10.1016/j.ejphar.2018.02.049.

Shin, E.J., Tran, H.Q., Nguyen, P.T., Jeong, J.H., Nah, S.Y., Jang, C.G., Nabeshima, T., Kim, H.C., 2018. Role of mitochondria in methamphetamine-induced dopaminergic neurotoxicity: involvement in oxidative stress, neuroinflammation, and Pro-apoptosis-A review. Neurochem. Res. 43 (1), 66–78. https://doi.org/10.1007/s11064-017-2318-5.

Stroet, M., Caron, B., Visscher, K.M., Geerke, D.P., Malde, A.K., Mark, A.E., 2018. Automated topology builder version 3.0: prediction of solvation free enthalpies in water and hexane. J. Chem. Theor. Comput. 14 (11), 5834–5845. https://doi.org/10.1021/acs.jctc.8b00768.

Sulzer, D., Rayport, S., 1990. Amphetamine and other psychostimulants reduce pH gradients in midbrain dopaminergic neurons and chromaffin granules: a mechanism of action. Neuron 5 (6), 797–808. https://doi.org/10.1016/0896-6273(90)90339-h.

Swift, M.L., 1997. GraphPad prism, data analysis, and scientific graphing. J. Chem. Inf. Comput. Sci. 37 (2), 411–412. https://doi.org/10.1021/ci960402j.

Torrie, G.M., Valleau, J.P., 1977. Nonphysical sampling distributions in Monte Carlo free-energy estimation: umbrella sampling. J. Comput. Phys. 23 (2), 187–199. https://doi.org/10.1016/0021-9991(77)90121-8.

Tunstall, B.J., Ho, C.P., Cao, J., Vendruscolo, J.C.M., Schmeichel, B.E., Slack, R.D., Tanda, G., Gadiano, A.J., Rais, R., Slusher, B.S., Koob, G.F., Newman, A.H., Vendruscolo, L.F., 2018. Atypical dopamine transporter inhibitors attenuate compulsive-like methamphetamine self-administration in rats. Neuropharmacology 131, 96–103. https://doi.org/10.1016/j.neuropharm.2017.12.006.

Venable, R.M., Brown, F.L.H., Pastor, R.W., 2015. Mechanical properties of lipid bilayers from molecular dynamics simulation. Chem. Phys. Lipids 192, 60–74. https://doi.org/10.1016/j.chemphyslip.2015.07.014.

Verónica, S., Evan, L.R., Yvette, V.U., Glen, R.H., Annette, E.F., 2001. Methamphetamine-induced rapid and reversible changes in dopamine transporter function: an in vitro model. J. Neurosci. 21 (4), 1413. https://doi.org/10.1523/JNEUROSCI.21-04-01413.2001.

Wanderlingh, U., Branca, C., Crupi, C., Conti Nibali, V., La Rosa, G., Rifici, S., Ollivier, J., D'Angelo, G., 2017. Molecular dynamics of POPC phospholipid bilayers through the gel to fluid phase transition: an incoherent quasi-elastic neutron scattering study. J. Chem. 2017 (1), 3654237. https://doi.org/10.1155/2017/3654237.

Wong-Ekkabut, J., Karttunen, M., 2016. Molecular dynamics simulation of water permeation through the alpha-hemolysin channel. J. Biol. Phys. 42 (1), 133–146. https://doi.org/10.1007/s10867-015-9396-x.

Yang, X., Wang, Y., Li, Q., Zhong, Y., Chen, L., Du, Y., He, J., Liao, L., Xiong, K., Yi, C.X., Yan, J., 2018. The main molecular mechanisms underlying Methamphetamine-induced neurotoxicity and implications for pharmacological treatment. Front. Mol. Neurosci. 11, 186. https://doi.org/10.3389/fnmol.2018.00186.

Zhang, X., Wang, Y., Wang, H., Li, H., Zhang, T., Peng, Y., Wang, X., 2020. Exploring methamphetamine nonenantioselectively targeting toll-like receptor 4/myeloid differentiation protein 2 by in silico simulations and wet-lab techniques. J. Chem. Inf. Model. 60 (3), 1607–1613. https://doi.org/10.1021/acs.jcim.9b01040.

Zhou, M., Cheng, K., Jia, G.-z., 2017. Molecular dynamics simulation studies of dopamine aqueous solution. J. Mol. Liq. 230, 137–142. https://doi.org/10.1016/j.molliq.2016.11.079.

Zorova, L.D., Popkov, V.A., Plotnikov, E.Y., Silachev, D.N., Pevzner, I.B., Jankauskas, S. S., Babenko, V.A., Zorov, S.D., Balakireva, A.V., Juhaszova, M., Sollott, S.J., Zorov, D.B., 2018. Mitochondrial membrane potential. Anal. Biochem. 552, 50–59. https://doi.org/10.1016/j.ab.2017.07.009.